Tin(IV) sulfide–alkylamine composite mesophase: a new class of thermotropic liquid crystals

Tong Jiang and Geoffrey A. Ozin*

Materials Chemistry Research Group, Chemistry Department, 80 St. George Street, University of Toronto, Toronto, Ontario, Canada, M5S 3H6

The synthesis, structural characterization, thermal, electronic, optical birefringence and electrical properties of a new class of semiconducting tin sulfide based thermotropic liquid crystals (LCs), Meso-SnS-*n*, are described for the first time. The as-synthesized crystalline form of Meso-SnS-1 has a structure that is based upon well registered yet poorly ordered porous tin(IV) sulfide layers between which are sandwiched well organized hexadecylamine bilayers. On warming this material to around 45 °C the hexadecylamine bilayer first becomes disordered while the porous tin(IV) sulfide sheets remain registered. This is followed, around 85 °C, by a transition where both the alkylamine bilayer and the porous tin(IV) sulfide lamellae become liquid crystalline at which point the intralayer but not the interlayer registry is lost. The liquid-crystal organic–inorganic composite phase has either a nematic or smectic C structure. Electrically, the room-temperature ordered phase has a conductivity of $5.3 \times 10^{-8}\ \Omega^{-1}\ cm^{-1}$ which increases by more than a 1000 times on transforming to the LC phase where it behaves as a semiconducting metallogen. The conductivity of Meso-SnS-1 cycles reversibly with temperature and displays discontinuities that are coincident with the crystal–semiliquid crystal and semiliquid crystal–liquid crystal thermal transitions that are defined by differential scanning calorimetry and variable-temperature powder X-ray diffraction. Meso-SnS-1 readily forms electrically conducting thin films which are able to reversibly adsorb molecules like H_2O and CO_2. These properties bode well for the use of this new class of inorganic semiconducting LCs for electro-optical displays and chemical sensing applications.

Liquid crystals (LC) represent a state of matter with properties between solid and isotropic liquid states.[1] Reinitzer first discovered the liquid crystalline state in 1888 when he was studying cholesterol esters that exist in plants and animals.[2] Subsequently Lehmann discovered, by polarized optical microscopy, that the opaque liquid phase was birefringent and intuitively attributed this property to the nature of the elongated structure of the ester molecules. The idea of using LCs in electro-optical display technology was first introduced in the 1960s. Since then, the LC field has experienced an explosive growth and some 70 000 LC compounds have now been synthesized.[3] A diverse range of new applications of LC materials are envisaged and under development.[4] Different LC phases may be identified in a polarizing optical microscope with a variable-temperature hot stage. Depending on the phase type and orientation of the sample, characteristic optical birefringence patterns, called 'textures', may be observed and used to identify LC phase types.[5]

Classes of materials that display LC properties are diverse. The most common group is based on simple rod- or disk-shaped organic molecules. Polymer LCs are another familiar group, in which the mesogenic units can be built into the polymer backbone or be attached as a side-arm.[6] LC polymers are used as precursors for the synthesis of ultra-high-strength fibers like Kevlar. The lower viscosity of liquid-crystal dendrimers compared to normal LC polymers offers faster switching for device applications.[7] The attractive optical, electrical and magnetic properties of metal- and metal cluster-containing LCs provide many interesting research and development opportunities.[8] For example, ionic metallogens are expected to have interesting charge transport properties.[9]

In this article, organic mesogenic components have, for the first time, been sandwiched between flexible inorganic porous tin sulfide layers to generate a novel class of composite metallogen. The synthesis, structural characterization, thermal, electronic, optical birefringence and electrical properties of this new class of semiconducting tin sulfide thermotropic liquid crystals, denoted Meso-SnS-*n*, are described. The liquid-crystalline state of Meso-SnS-1 is investigated using differential scanning calorimetry (DSC), variable-temperature powder X-ray diffraction (VT-PXRD), hot-stage polarized optical microscopy (POM), and electrical transport measurements.

Results and Discussion

Synthesis

Water-soluble $SnCl_4 \cdot 5H_2O$ and $(NH_4)_2S$ salts are used as tin and sulfur sources. Aqueous ammonia solution is added to adjust the pH of the reaction mixture. A variation of the composition of the initial reaction mixture, pH, crystallization temperature and time give rise to a series of materials with the largest *d*-spacing ranging from 20 to 51 Å as detected by PXRD. The material with the largest *d*-spacing of 51 Å, denoted Meso-SnS-1, was chosen for the pilot-study described in this paper. The chemical composition of this material was established by elemental analysis to be: Sn, 15.6%; S, 8.74%; C, 59.1%; N, 4.5%; H_2O, 5.27%. This translates into an empirical formula of $Sn_{1.00}S_{2.07}(HDA)_{2.34}(H_2O)_{2.23}$ (C% was used in this calculation, HDA denotes hexadecylamine). When Meso-SnS-1 was washed with an excess of acetone, it transformed to a series of new phases with the largest *d*-spacings reduced to 31–24 Å, discussed in more detail below. Thus special care has to be taken if phase pure Meso-SnS-1 is desired. When the same reaction mixture was crystallized at room temperature for a period of 19 days, a white product was created, denoted Meso-SnS-2.

Structure characterization

Powder X-ray diffraction (PXRD), scanning and transmission electron microscopy (SEM, TEM). The powder XRD pattern of Meso-SnS-1 is shown in Fig. 1. The first diffraction peak, assumed to be (001), corresponds to a *d*-spacing of about 51 Å. Reflections up to the 11th order of the (001) diffraction are observed. Beside the (00*l*) series, no other diffraction peaks are observed in the low-angle diffraction region. The reflections

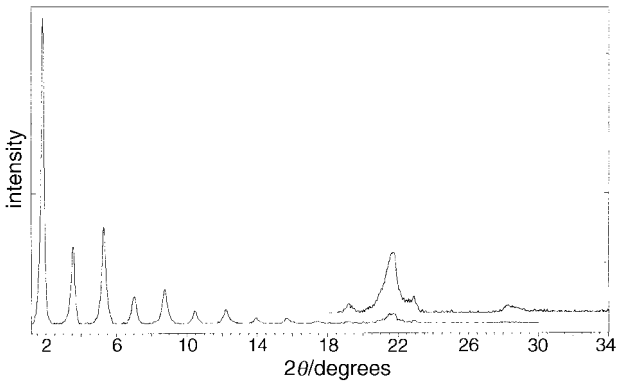

Fig. 1 PXRD pattern of Meso-SnS-1

between 2θ 20 and 24° and at 2θ *ca.* 28° can only be detected when a highly ordered (00*l*) family is present. Clearly, the powder XRD pattern of Meso-SnS-1 displays the characteristics of a well ordered layered structure with evidence of registry between the sheets. The flaky morphology of this material, as displayed in the SEM image, Fig. 2(*a*), supports this proposal. A TEM image of this material (direct imaging through a thin section of the material), however, reveals what appears to be a hexagonal array of pores with a center-to-center distance of *ca.* 50 Å, as illustrated in Fig. 2(*b*). A TEM image (epoxy-embedded material, microtomed thin section) recorded orthogonally to the hexagonally patterned layers of the same material reveals evidence of a lamellar architecture, Fig. 2(*c*). Combining the information obtained from the PXRD, SEM and TEM images, Meso-SnS-1 is best described as a porous mesolamellar tin(IV) sulfide with hexadecylamine bilayers sandwiched between the layers, an illustration of which is depicted in Fig. 3 (top). The hydrocarbon tails from the

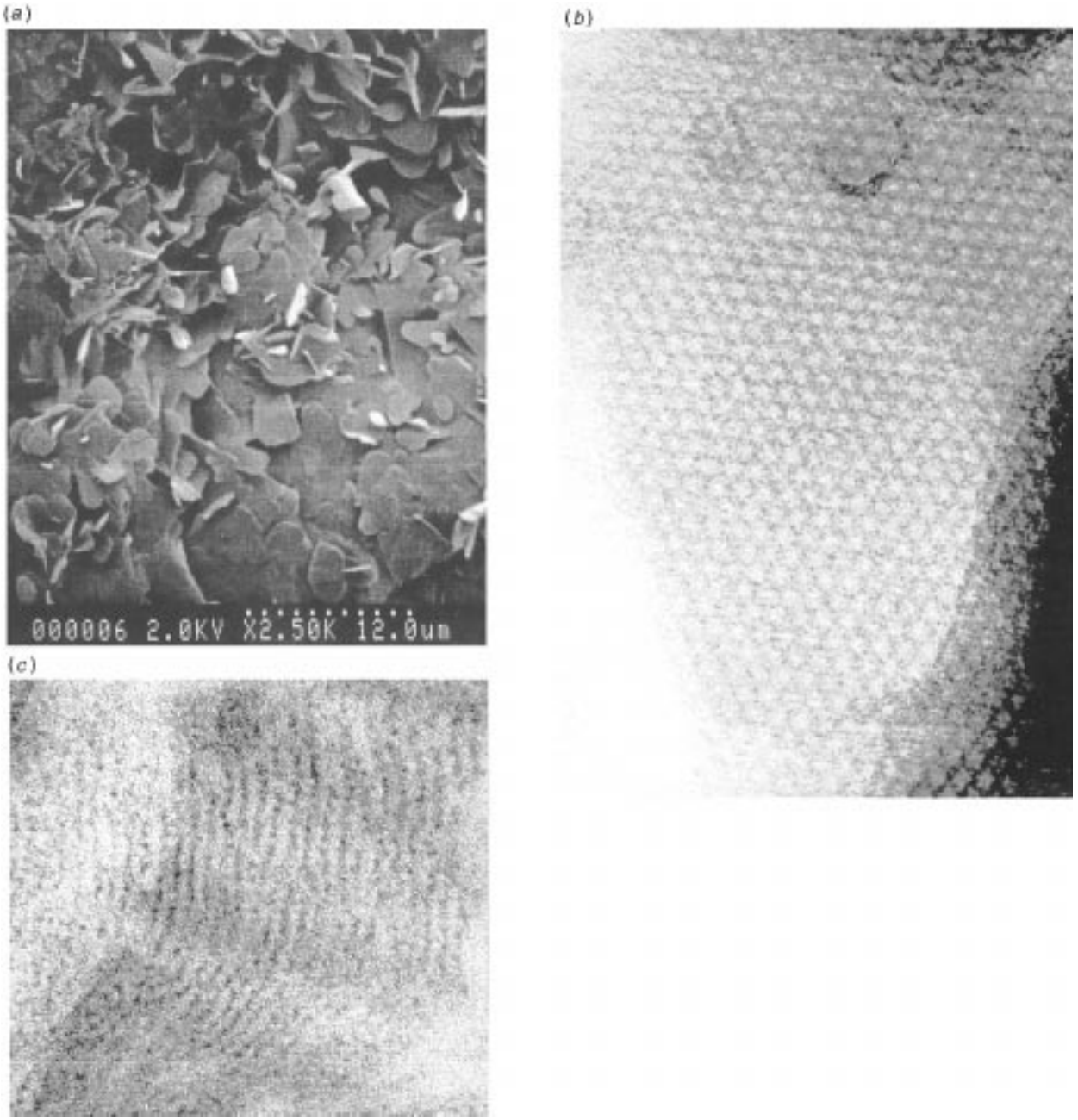

Fig. 2 (*a*) A representative SEM image of Meso-SnS-1. (*b*) A TEM image of the tin(IV) sulfide layer (magnification 976 000 ×, powder on carbon film, direct imaging, structural repeat *ca.* 50 Å). (*c*) A TEM image orthogonal to the tin(IV) sulfide layer showing the lamellae (magnification 540 000 ×, microtomed cross-section, structural repeat *ca.* 50 Å).

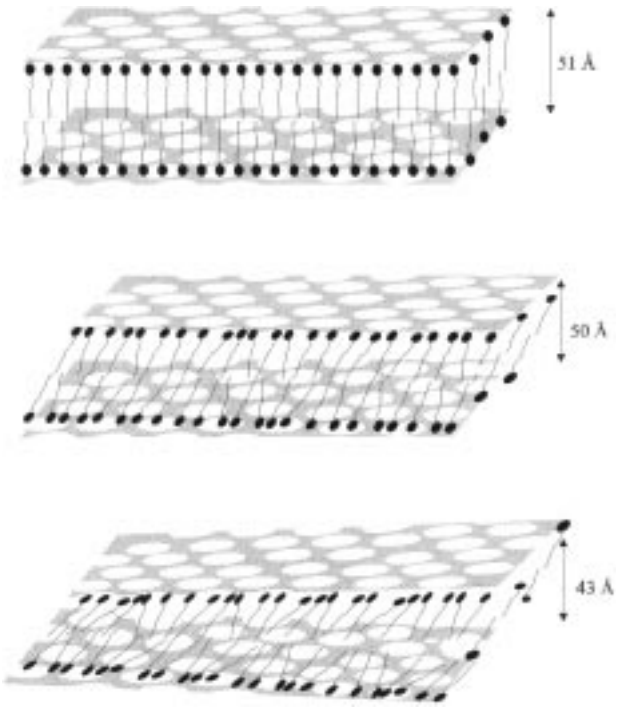

Fig. 3 Illustration of the structures of the as-synthesized crystalline porous layer form of mesomorphic tin(IV) sulfide (top) and its semi-liquid (middle) and liquid-crystalline (bottom) phases. On warming the material the alkylamine bilayer first becomes disordered around 45 °C while the porous tin(IV) sulfide sheets remain more-or-less registered (middle), and then around 85 °C both the alkylamine bilayer and the porous tin(IV) sulfide lamellae become liquid crystalline at which point the intralayer but not the interlayer registry is lost (bottom). The liquid-crystal organic–inorganic composite phase has either a nematic or a smectic C structure.

hexadecylamine double layers are expected to interact with each other through hydrophobic van der Waals forces and the amine head groups interact with the tin sulfide layer. The 5.9% water in Meso-SnS-1 determined by elemental analysis, presumably reside within the pores and between the tin sulfide layers and most likely hydrogen-bond with the hexadecylamine head group and possibly the sulfide in the tin sulfide layers, as found in microporous layer tin(IV) sulfides[10] and to be further discussed below. Note that the thickness of tin(IV) sulfide sheets in dense berndtite SnS_2,[12] microporous SnS-*n* (*n* refers to structure type)[10,11] and $Cs_4Sn_5S_{12}$[13] are all found to be *ca.* 6 Å. The length of a fully extended hexadecylamine bilayer can be estimated to be *ca.* 45 Å. By comparison, in the octadecylamine-bilayer intercalated 2H-TaS_2,[14] the fully extended organic bilayer spacing was found to be 50 Å and the contribution from each C was estimated to be *ca.* 1.26 Å.[15] The X-ray reflections between 20 and 24° (2θ) in Fig. 1 are best assigned to positional ordering of the hexadecylamine molecules within the bilayer.[16] Crystalline hexadecylamine displays a very similar PXRD pattern in this range. As will be shown later, these reflections are temperature sensitive and diminish as the material undergoes transformations from its crystalline to liquid-crystalline states. The broad diffraction peak at 28° (3.15 Å) appears to be associated with order in the tin(IV) sulfide sheets, as discussed below.

Interestingly, the octadecylamine (ODA) bilayer intercalated TaS_2 has a composition of $(ODA)_{2/3}TaS_2$, that is, the ratio of octadecylamine: TaS_2 is 0.667. In $(HDA)_{2.34}SnS_{2.07}$, the ratio of HDA: $SnS_{2.07}$ is 2.34. The layered structure of 2H-TaS_2 is similar to that of bulk SnS_2, except that the Ta^{IV} centers are located in trigonal-prismatic, rather than octahedral, sites between two hexagonally close-packed sulfur slabs to form a sandwich structure. The unit-cell parameters are 3.3 Å for *a* and *b* and 6.0 Å for *c* in 2H-TaS_2;[17] while 3.6 Å for *a* and *b* and 5.9 Å for *c* in 2H-SnS_2.[12]

If one assumes that the amine molecules in the $(ODA)_{2/3}TaS_2$ and $(HDA)_{2.34}SnS_{2.07}$ materials are similarly close-packed, the considerably lower tin(IV) sulfide content in the Meso-SnS-1 suggests a much less densely structured or highly porous tin(IV) sulfide layer, with respect to the dense packed layers of bulk TaS_2 or SnS_2. This is consistent with the TEM images shown above in Fig. 2 (*b*), (*c*), which exhibits hexagonal arrays of pores in the tin sulfide layer of Meso-SnS-1. The packing density of the tin sulfide constituent layer in Meso-SnS-1 may be estimated to be only 29% (0.67/2.34) of that of the densely packed TaS_2 layer. The packing density of tin sulfide layers in various tin sulfide materials may be expressed by the number of tin atoms per unit area of sheet surface. The packing density of the microporous tin sulfide layer in ATEA-SnS-1, $(NH_3)_{0.5}(Et_4N)_{1.5}Sn_3S_7$[10] can then be calculated to be 0.034 Sn $Å^{-2}$, while that of the densely packed tin sulfide layer in SnS_2 is 0.076 Sn $Å^{-2}$. This implies that the packing density of the porous tin sulfide layer of ATEA-SnS-1 is 45% of that of bulk SnS_2. This suggests that the Meso-SnS-1 is less densely packed or more porous than even the microporous layered material ATEA-SnS-1. Note that in addition to $(ODA)_{2/3}TaS_2$, an interdigitated intercalation compound $(ODA)_{1/3}TaS_2$ has also been reported with a tantalum sulfide interlamellar spacing of 34 Å.[18] Therefore, layered tin sulfide materials with interlamellar distances of 30–24 Å, Fig. 4, formed through acetone-washing of the Meso-SnS-1 at room temperature, may be assigned to porous tin sulfide layers with interdigitated hexadecylamine bilayers between the interlamellar gap.

Spectroscopy. As revealed by PXRD, SEM and TEM, as-synthesized Meso-SnS-1 features a porous layered tin(IV) sulfide structure with a fully extended hexadecylamine bilayer sandwiched in the interlamellar gap. The porosity of the tin sulfide sheet in Meso-SnS-1 is greater than that in ATEA-SnS-1. In known close-packed and open-framework tin(IV) sulfides, the most common coordination environments for a tin(IV) center is tetrahedral, pseudo-bipyramidal and octahedral.[10–12] A pertinent question is whether the tin(IV) center in Meso-SnS-1 is six-coordinate like in bulk SnS_2, or five- or four-coordinate as in the microporous SnS-*n* materials. Local probe analytical techniques, such as solid-state ^{119}Sn, ^{13}C, ^{15}N NMR and FT Raman spectroscopies, have been used effectively in this study to address these structural questions, described below.

Solid-state magic angle spinning (MAS) NMR. The chemical shift of ^{119}Sn NMR is extremely sensitive to coordination number and has been successfully employed to probe the local

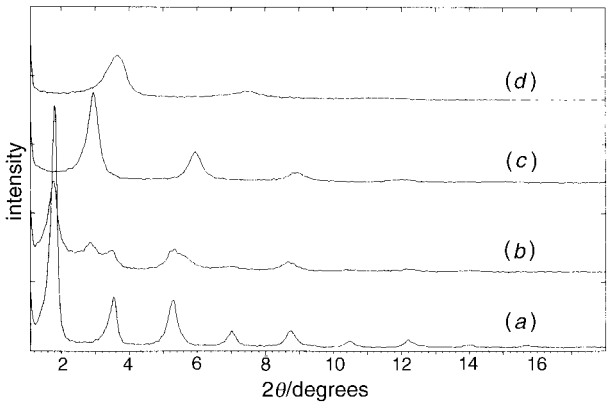

Fig. 4 PXRD patterns depicting the transformation of Meso-SnS-1 to new phases when exposed to acetone solvent: (*a*) Meso-SnS-1; (*b*) rinsed with acetone; (*c*) soaked in acetone for 20 min; (*d*) soaked in acetone overnight

coordination environment of tin.[19] In general, the ^{119}Sn NMR chemical shift moves to lower frequency or higher field with an increase of coordination number due to the enhancement of the effective electron density at tin. For example, the chemical shift for a tetrahedral tin(IV) sulfide was found to occur over a range δ 70 to -25, for pseudo-trigonal bipyramidal tin in the range $\delta-300$ to -360, and for octahedral tin in berndtite SnS_2 at $\delta-763.6$ (referenced to $SnMe_4$). The ^{119}Sn MAS NMR spectrum of Meso-SnS-1 is shown in Fig. 5. The two broad bands centered at $\delta-510$ and -750 clearly show the presence of two distinct tin sites in this material, presumably one five- and the other six-coordinate tin(IV). The chemical shift at $\delta-510$ is assigned to a five-coordinate tin(IV) site. In Meso-SnS-1, the five-coordinate tin(IV) site presumably has six-coordinate tin(IV) sites as neighbors, thus different bond lengths and angles, in comparison with known tin(IV) sulfides containing five-coordinate, pseudo-trigonal bipyramidal tin(IV) sites that have been studied by ^{119}Sn NMR.[10,19] For example, DABCOH-SnS-1 contains only one kind of five-coordinate, pseudo-trigonal bipyramidal tin(IV) site, the isotropic chemical shift (CS) of which occurs at $\delta-343.8$.[10] In addition, the five-coordinate tin(IV) in Meso-SnS-1 may adopt another coordination geometry, rather than pseudo-trigonal bipyramidal. These all can introduce a distinct chemical shift value. As an example, the isotropic CS value for the distorted T_d tin(IV) in dimeric $(CHA)_2Sn_2S_6$ (CHA cyclohexylammonium) and framework $Na_4Sn_3S_8$ is quite different, $\delta+67.6$ for the former, and $\delta-16$ for the latter.[10,19c] $Na_4Sn_3S_8$ is constituted by both distorted tetrahedral and trigonal-bipyramidal tin sites.[20] In addition, the molar ratio of S/Sn in Meso-SnS-1 as determined by elemental analysis is 2.07, which suggests that the tin(IV) sulfide sheet is negatively charged. Thus it is unlikely to be built-up entirely of six-coordinate tin(IV) as in neutral SnS_2.

The ^{15}N cross-polarization, CP MAS NMR spectrum of Meso-SnS-1, Fig. 5, also shows two chemical shifts $\delta-289$ and -342 (relative to $MeNO_2$). This implies that two types of hexadecylamine molecules are present in the sample, presumably a protonated and a neutral hexadecylamine. Additional support for this proposal stems from the ^{13}C CP MAS NMR spectrum of Meso-SnS-1 that is also displayed in Fig. 5 (scale expanded to show the weaker lines). This spectrum is also consistent with the presence of a negatively charged tin(IV) sulfide layer, and the co-existence of protonated and neutral hexadecylamines. In order to compensate the framework charge, some hexadecylamine molecules are expected to be protonated. To amplify, the band at δ 39–44 is assigned to the α-carbon on the amine head group. Note that the chemical shift of α- and β-carbons in liquid 1-decylamine occurs at δ 42.6 and 34.5. The presence of three overlapped signals at δ 42.8, 40.0 and 39.2 in the ^{13}C CP MAS NMR of Meso-SnS-1 may suggest three types of hexadecylamine in the sample, one neutral, one protonated to balance the framework charge and one interacting with adsorbed CO_2 (further discussed below). Neutral amines are known to be able to readily adsorb CO_2 and have been used in industry to remove CO_2 from gas streams. It is also known that amines can react with CO_2 in solution to form carbamates. Therefore, it is likely that the Meso-SnS-1 sample stored in air has adsorbed some CO_2. The ^{13}C CP MAS NMR of pure hexadecylamine stored in air shows two signals at δ 39.1 and 43.5, Fig. 5, one presumably corresponding to the free amine and the other to carbamate. There is a weak signal at δ *ca.* 160 in the ^{13}C CP MAS spectrum of Meso-SnS-1 which may correspond to adsorbed CO_2. As mentioned above, only two chemical shift signals were resolved in the ^{15}N CP MAS spectrum of Meso-SnS-1. This is likely attributed to the very low signal intensity and poor signal-to-noise ratio in Fig. 5, as a consequence of the low NMR sensitivity of ^{15}N. In addition, these different nitrogen sites may have different cross-polarization efficiency. No signal was observed from a ^{15}N MAS NMR measurement without CP. Note that the as-synthesized Meso-SnS-1 sample contains 5.9% occluded water molecules as determined by elemental analysis. Therefore, the adsorbed CO_2 may either react with the neutral hexadecylamine to form carbamates or react with amine and water through an acid–base type reaction.

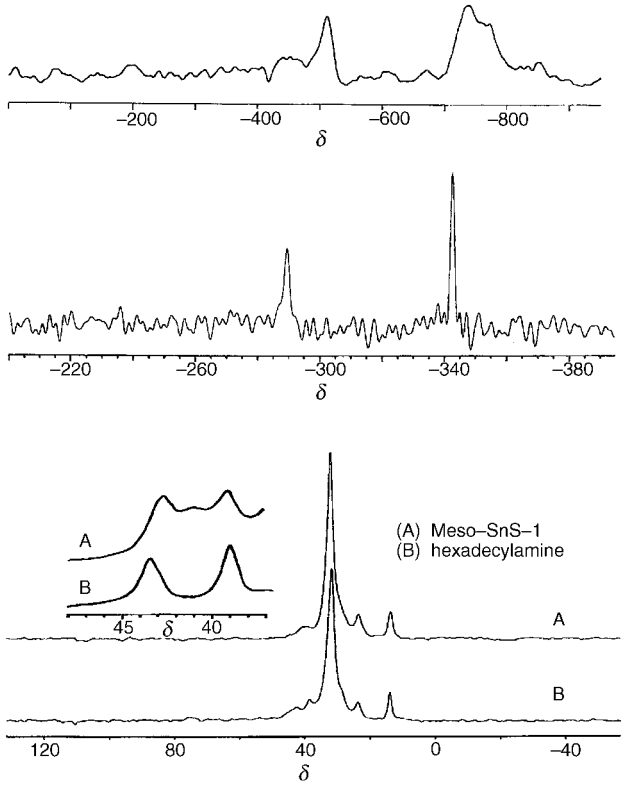

Fig. 5 ^{119}Sn MAS (top), ^{1}H–^{15}N CP MAS (middle) and ^{1}H–^{13}C CP MAS (bottom) NMR spectra of Meso-SnS-1

Raman spectroscopy. Two intense peaks at 322 and 351 cm^{-1} in the Raman spectrum of Meso-SnS-1, Fig. 6, also supports the existence of an additional tin(IV) site other than just six-coordinate tin(IV). As shown in Fig. 6, the Raman spectra of crystalline and amorphous forms of SnS_2 berndtite show only one strong Raman band at 317 cm^{-1}. The band at 351 cm^{-1} suggests the presence of a stronger and shorter Sn—S bond than that in octahedral SnS_6 sites. This implies the existence of a lower coordinated tin(IV) site in Meso-SnS-1 other than octahedral SnS_6 sites. This is consistent with the ^{119}Sn NMR results.

It is known that layered microporous tin(IV) sulfides like $Cs_4Sn_5S_{12}$,[13] can be built-up of five- and six-coordinate tin(IV).

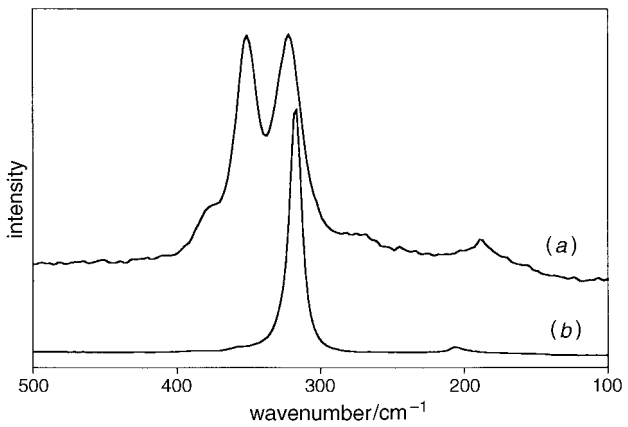

Fig. 6 FT-Raman spectra of Meso-SnS-1 (*a*) and crystalline berndtite SnS_2 (*b*)

In $Cs_4Sn_5S_{12}$, the basic building unit is corner-sharing Sn_3S_4 broken-cube cluster pairs. They are linked together by double sulfide $(\mu\text{-}S)_2$ bridge bonds to form parallel-stacked microporous layers. It can be imagined that various tin(IV) sulfide layer topologies can be built from similar building blocks. It is interesting that the tin–tin distance in the broken cube clusters is 3.611 Å, which in a hexagonal unit cell may translate to a *d*-spacing of 3.15 Å as found in SnS_2 berndtite. Therefore, the presence of the broad diffraction peak at 3.15 Å in Fig. 1, is consistent with a tin(IV) sulfide porous layer structure built up of broken-cube clusters. It should be noted that the line broadening present in the ^{119}Sn NMR and Raman spectra and the lack of other diffraction peaks from the tin(IV) sulfide sheets, all indicate relatively poor ordering of the building units.

UV–VIS spectroscopy. The UV–VIS reflectance spectrum of the Meso-SnS-1 is shown in Fig. 7, together with DABCOH-SnS-1 and berndtite SnS_2. Like bulk SnS_2, the optical absorption edge in the Meso-SnS-1 corresponds to a $S^{-II}(3p) \rightarrow Sn^{IV}(5d)$ valence to conduction band electronic transition.[21] An increase of sulfur coordination around the tin(IV) center would presumably increase the overlap of tin and sulfur orbitals and reduce the bad gap, as discovered in various low-dimensional cadmium sulfide-based materials.[22] Consequently, a red-shifted optical absorption edge would result. The absorption edge of Meso-SnS-1 is found to be between those of DABCOH-SnS-1 [five-coordinate tin(IV)] and berndtite SnS_2 [six-coordinate tin(IV)]. This is consistent with a mixed five- and six-coordination environment around the tin(IV) centers. It should be mentioned that the coordination of sulfur is also expected to increase when increasing the coordination of tin as found for the known tin sulfides.

Mössbauer spectroscopy. Attempts to collect Mössbauer data for Meso-SnS-1 at room temperature failed to give a well defined signal. Mössbauer data can only be obtained for rigid structures which have a high recoil-free fraction. For example, SnS-1 materials with 24-atom rings within the tin(IV) sulfide layer give sufficient intensity and low signal/noise at room temperature for data collection, fitting and quantitative analysis, whereas SnS-3 materials with 32-atom rings provide low-quality data which is not useful for quantitative analysis.[10] The absence of a Mössbauer signal at room temperature suggests that the tin sulfide layer in Meso-SnS-1 is highly deformable and appears to be even more flexible than that found in SnS-3 materials. This is consistent with the proposed porous layer topology for the mesostructured tin sulfide framework of Meso-SnS-1. Low-temperature studies are planned.

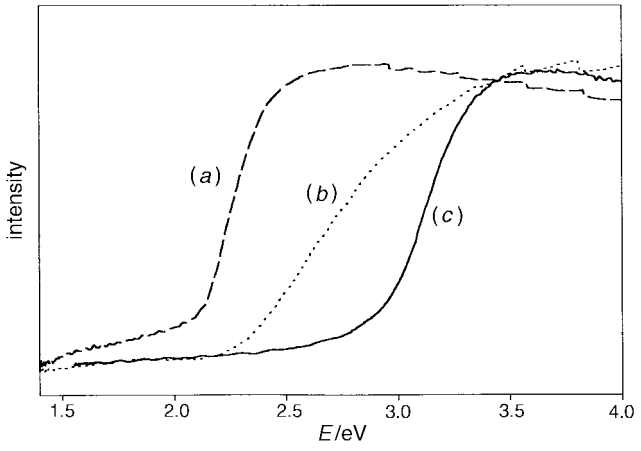

Fig. 7 UV–VIS absorption spectra of some 2D tin(IV) sulfides: (*a*) SnS_2; (*b*) Meso-SnS-1; (*c*) DABCOH-SnS-1

Thermal properties

Thermogravimetry (TG). The liquid crystalline properties of the Meso-SnS-1 material were revealed by a combined TG, DSC, *in situ* VT-PXRD and hot-stage polarized optical microscopy, POM, study. The TGA trace of Meso-SnS-1 was recorded under nitrogen with a heating rate of 5 °C min^{-1} between room temperature and 600 °C, Fig. 8. The first thermal event occurred at *ca.* 90 °C with a mass loss of 2.9%. It was followed by two continuous thermal events between 180 and 300 °C and 300–600 °C with a mass loss of 56.3 and 21.8%, respectively. The total mass loss from 20 to 600 °C was determined to be 81%.

Differential scanning calorimetry (DSC). The DSC trace of this material under nitrogen between 20 and 110 °C is displayed in Fig. 9(*a*). The first heating cycle features two main overlapping endothermic processes with a total enthalpy (ΔH) of 114.4 J g^{-1} between 60 and 100 °C. On cooling, two overlapping exothermic events take place between 95 and 70 °C with a total ΔH of -26.7 J g^{-1}, in addition to a single sharp thermal event around 28 °C with an enthalpy of -29.5 J g^{-1}. In the second heating cycle, a new sharp endotherm is developed at 42 °C ($\Delta H = 27.0$ J g^{-1}), corresponding to the exothermic process at 28 °C. The endotherms between 75 and 95 °C display a reduced enthalpy of 22.8 J g^{-1} in comparison with the first heating cycle. Subsequently, the DSC trace is fully reversible over multiple cycles.

The difference observed between the first and second heating cycles is most likely attributed to the removal of adsorbed molecules such as CO_2 and H_2O during the first heating cycle which corresponds to a mass loss of 2.9% as determined by TG. As mentioned earlier, neutral amines are known to be able to adsorb CO_2 from air. It was found during this study that leaving the thermally cycled DSC sample in a loosely sealed aluminium sample holder at room temperature in air for 9 days, the first endothermic transition moves back to its initial high temperature above 60 °C with a concomitant growth of ΔH, Fig. 9(*b*), whereas the succeeding exothermic and endothermic processes remain almost invariant as found in Fig. 9(*a*). This result suggests that re-adsorption of guest molecules like CO_2 and H_2O from air may have occurred at room temperature. Interestingly, the presence of guest molecules has also significantly shifted the first thermal event (at 42 °C for an out-gassed sample) to higher temperature (*ca.* 80 °C for an as-synthesized sample), the origin of which will be addressed shortly.

***In situ* variable-temperature (VT) PXRD measurements.** As revealed from the DSC trace, an outgassed Meso-SnS-1 sample undergoes two major reversible thermal events at 42 and 75–95 °C, with an averaged enthalpy of 28.3 J g^{-1} for the

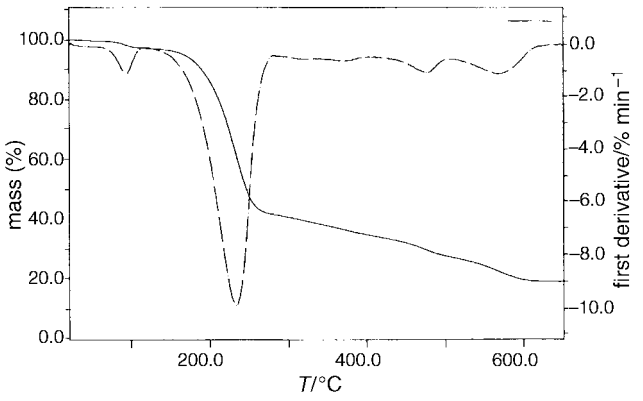

Fig. 8 TG trace of Meso-SnS-1 recorded in nitrogen with a heating rate of 5 °C min^{-1}

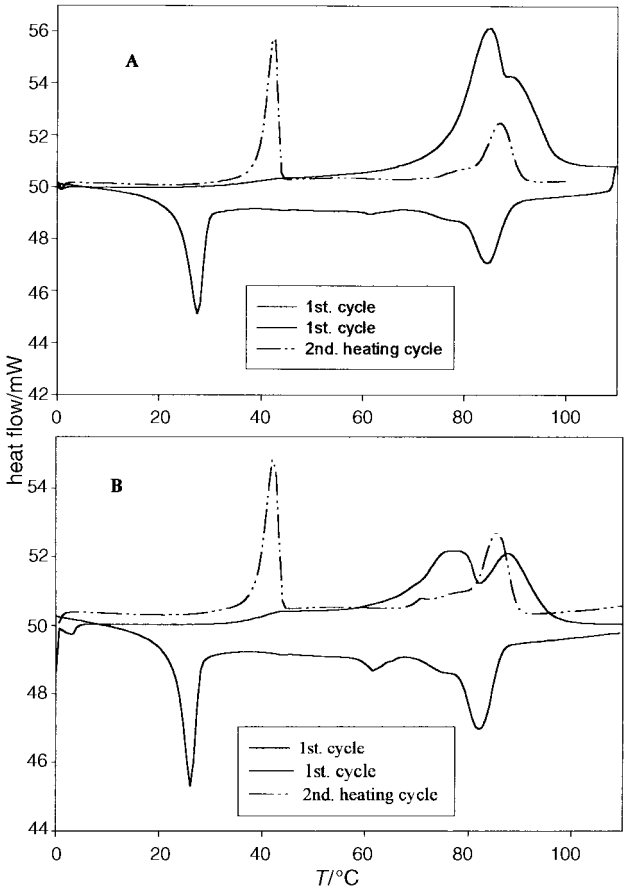

Fig. 9 DSC traces of Meso-SnS-1: (A) an as-synthesized sample; (B) sample (A) left in the aluminium DSC sample holder at room temperature in air for 9 days. Recorded with a heating rate of 5 °C min^{-1}.

former, and 24.8 J g^{-1} for the latter. The related structural change of Meso-SnS-1 is investigated by *in situ* VT-PXRD under a nitrogen atmosphere. As displayed in Fig. 10, starting from an as-synthesized Meso-SnS-1 sample, essentially no variation of the PXRD pattern takes place up to 55 °C. At 75 °C following the first thermal event observed in the DSC trace (the first heating cycle), the diffraction peaks relating to the positional order of the hexadecylamine bilayers coalesce to a single broad peak around 2θ 20.5°. The (00*l*) diffraction series display a slight shift to higher 2θ. This implies that the positional ordering of the hexadecylamine bilayer has become disrupted at the first thermal event. Following the second thermal event in the DSC trace (the first heating cycle), the (00*l*) peaks shift considerably to higher 2θ and display a smaller number of diffraction orders. Meanwhile the broad diffraction peak at $2\theta = 20.6°$ has vanished. Apparently at the second thermal process, the positional arrangement of the hexadecylamine bilayer has become completely disordered and the registry of the tin sulfide lamellae has become disrupted. The tin sulfide interlamellar distance has contracted by 8 Å at 100 °C. Cooling the sample to 50 °C reverses the change observed at 100 °C. Further cooling of the sample to room temperature reverses the change that occurred at 75 °C. As observed in the DSC trace, the second heating cycle reverses the occurrences observed during the first cooling cycle. Subsequently, the whole process is reversible over many cooling and heating cycles. It is interesting that after the first heating–cooling cycle, the PXRD pattern of the sample and its interlamellar spacing remain invariant as those of the as-synthesized Meso-SnS-1, although some physisorbed CO_2 and H_2O molecules have been removed from the latter as discussed above. This indicates that the adsorbed guest molecules reside within

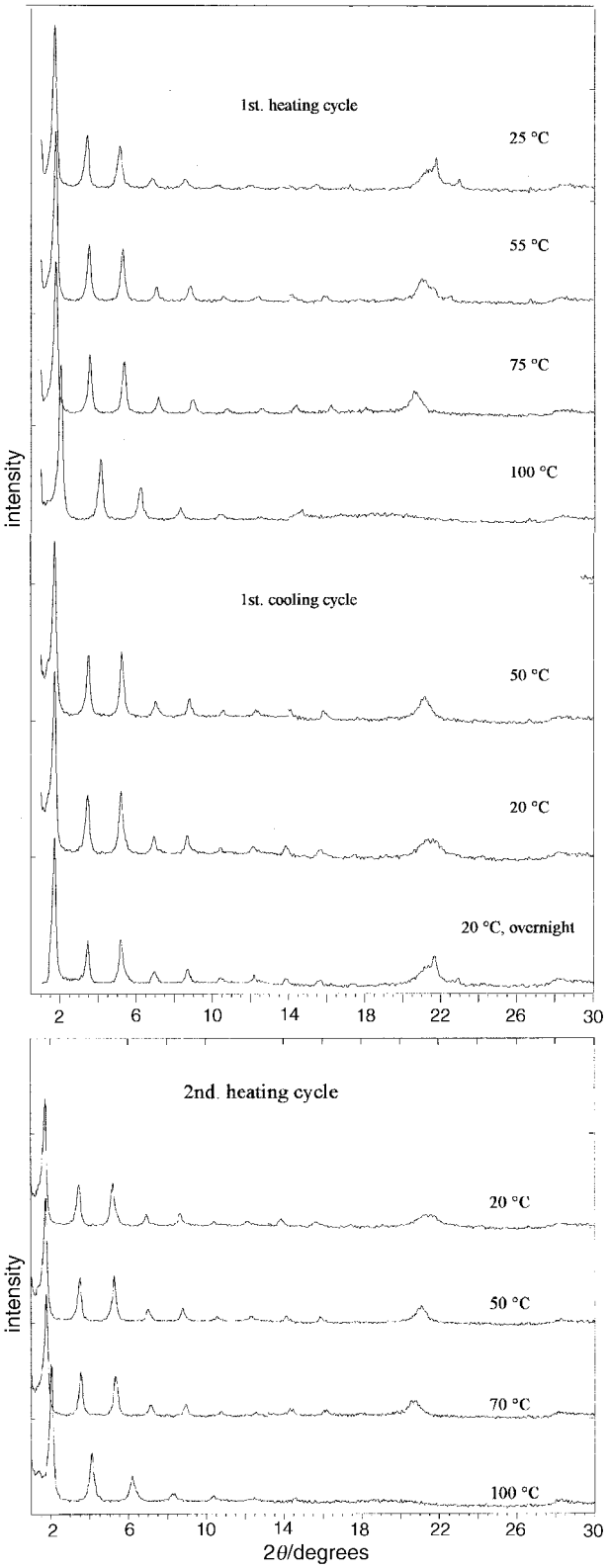

Fig. 10 *In situ* VT-PXRD patterns of Meso-SnS-1 recorded in a nitrogen atmosphere

the pores of the tin(IV) sulfide sheet, therefore their adsorption–desorption does not affect the interlamellar spacing. The adsorbed CO_2 and H_2O molecules are expected to interact with the head group of the hexadecylamine bilayer through an acid–base interaction and likely to generate a hydrogen-bonded network. This is expected to enhance the interactions between the hexadecylamine molecules and their interactions with the tin(IV) sulfide layers and 'lock' them in place, thereby shifting the thermally induced disruption of the positional

order of the hexadecylamine bilayers to higher temperature, as observed. Note that if the adsorption of CO_2 and H_2O occurs on the external surface of the crystallites, it should not affect the thermal behaviour of the Meso-SnS-1 sample, especially the thermal transition temperature of the hexadecylamines.

Unlike pure hexadecylamine which becomes an isotropic liquid at 41 °C, the hexadecylamine bilayer confined between the tin sulfide sheet starts to loose positional order at this temperature, however still retaining the orientational order along the long molecular axis. At 75 °C, it surrenders the positional order completely but maintains the orientational order with the molecular long axis tilted relative to the tin sulfide layer normal. Meanwhile the stacking of the tin(IV) sulfide layer remains well ordered at the first thermal transition, and only becomes disrupted at the second thermal transition. Clearly, the Meso-SnS-1 has lost certain positional order and gained some mobility at this temperature, which is characteristic of a liquid-crystalline state.

The thermotropic liquid-crystal character of the Meso-SnS-1 material is further revealed by a hot-stage optical microscopy study. 'Melting' of this material into a fluid-like state was observed at *ca.* 90 °C in air, the second thermal transition temperature. A thin, transparent yellow film can be readily produced at this temperature by gently pressing the material between glass cover slides. A characteristic Schlieren optical birefringence texture was observed under crossed polarizers, Fig. 11. The fine and busy texture make it difficult to establish whether the liquid crystal phase is smectic C or nematic. The texture is akin to that expected for a nematic phase, however, the PXRD pattern clearly displays the (00*l*) family of reflections diagnostic of a layered material with no positional order and suggests smectic C. If the material is truely nematic, it would imply that the order of the tin(IV) sulfide layers is retained in the mesogenic stage with the hexadecylamine bilayers/molecules likely extending through the pores of the tin(IV) sulfide sheets after the adsorbed guest molecules have been partially removed. Additional studies, such as X-ray scattering and deuterium wide-line NMR, are required to determine the phase identity of the mesomorphic tin(IV) sulfide material. The material transforms to the SnS_2 berndtite phase before it reaches the isotropic state, as to be described below.

The contraction of the interlamellar spacing observed by *in situ* VT-PXRD with heating and reversal on cooling, is best assigned to the tilting of the hexadecylamine bilayer from its fully extended vertical position, with respect to the tin(IV) sulfide layers.[15] The tilt angle can be calculated according to the simple geometry illustrated in Fig. 12. An abrupt increase of the tilting angle and decrease of the interlamellar distance occur at the second thermal event. This may be partly attributed to the extension of hexadecylamine into the pores and/or undulation of the tin sulfide layer if a nematic phase is obtained at this temperature. However, if it is a smectic C phase, then it is most probably entirely due to the tilting of the hexadecylamine bilayers relative to the tin sulfide layer normal. These ideas are encapsulated in the schematic illustration of the crystal→semi-LC→LC structural transformations shown in Fig. 3.

It is interesting to mention that further heating of the sample to 120 °C and collecting a PXRD pattern at that temperature, then cooling back to room temperature, leads to an apparently irreversible transformation of the Meso-SnS-1 to a new phase which has a reduced interlamellar distance of 30 Å at room temperature, Fig. 13. The diffraction pattern of this new phase displays a considerable line broadening in comparison with the original Meso-SnS-1 material. It undergoes a reversible thermal expansion between room temperature and 100 °C, with an interlamellar distance of 30 Å at room temperature and 36 Å at 100 °C. In contrast to the original Meso-SnS-1 phase, it displays a larger interlamellar distance, that is, the alkylamine bilayer tilts towards the layer normal at higher

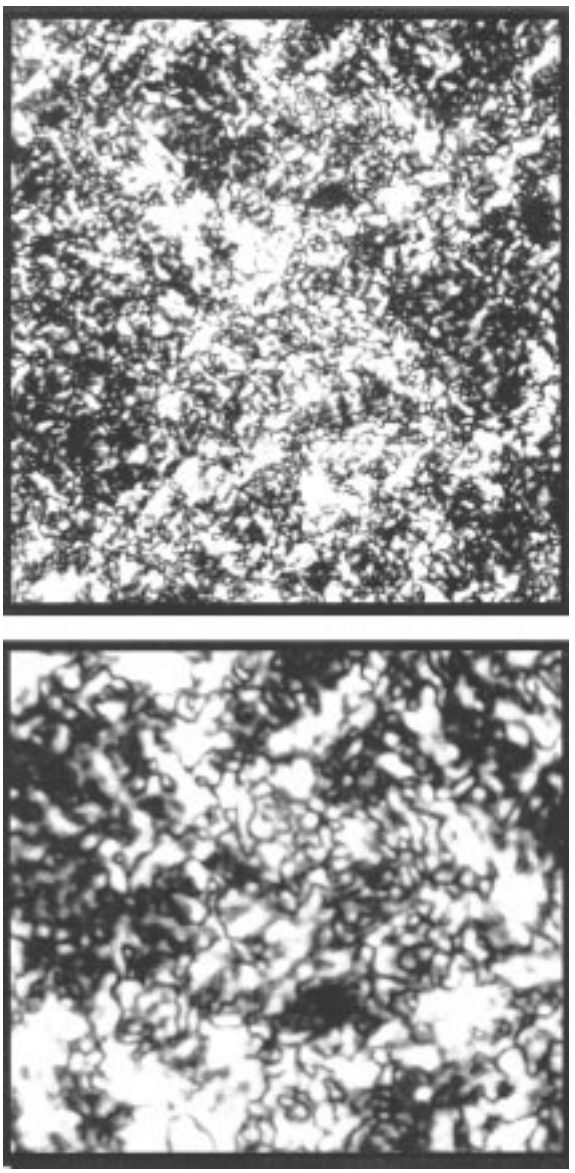

Fig. 11 Schlieren optical birefringence texture of Meso-SnS-1 obtained in a polarizing optical microscope, using converging white light and cross-polarizers. Top: low magnification; bottom: higher magnification image.

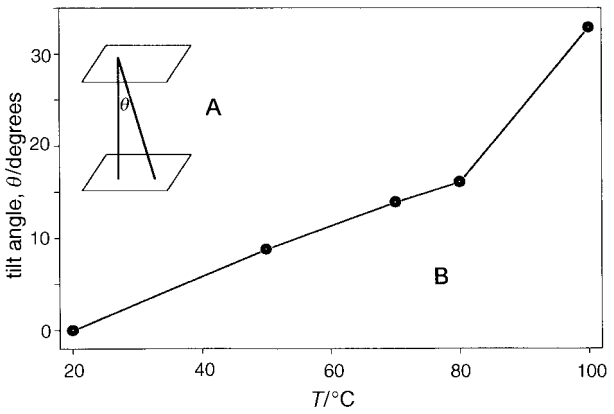

Fig. 12 (A) A schematic representation of the tilted hexadecylamine bilayer with respect to the tin sulfide layer and (B) a plot of the alkylamine bilayer tilt angle *vs.* temperature in Meso-SnS-1

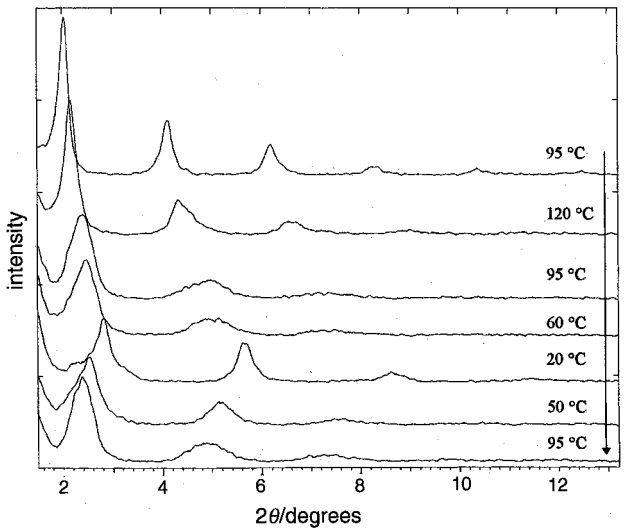

Fig. 13 *In situ* VT-PXRD patterns of Meso-SnS-1 recorded under nitrogen

temperature. Interestingly, on heating the sample to 120 °C and keeping it horizontal, the Meso-SnS-1 phase is found to retain the PXRD pattern typical of the Meso-SnS-1, with the first diffraction peak at *ca.* 51 Å and diffracting up to the 10th order, obtained after cooling it back to room temperature! In addition, between 100 and 140 °C the DSC trace of Meso-SnS-1 does not show any detectable exothermic and endothermic processes, and the TG trace does not display any mass loss either. This suggests that the seemingly irreversible phase change that occurred at 120 °C shown in Fig. 13, is due to the mechanical motion of the material caused by the movement of the sample holder during the PXRD data collection. Note that the Siemens D5000 diffractometer that was used in this study has a $\theta/2\theta$ configuration. It appears that a shear motion has occurred at the mesogenic stage of the Meso-SnS-1 material that is induced by the mechanical tilting and flow of the sample. Presumably the shear forces cause the hexadecylamine to tilt significantly away from the layer normal. It is well known that thermotropic liquid crystals may exhibit very high viscosity and display extremely lengthy relaxation times to attain thermodynamic equilibrium.[1,4,5] It is therefore possible that the shear induced transition creates a paramorphic 30 Å Meso-SnS-1 phase which if left long enough might slowly revert to the original 51 Å phase.

Thermal stability. The evolution of the PXRD pattern of the Meso-SnS-1 from room temperature to 100 °C was discussed above. From 100 to 180 °C, a further shrinkage of the layer spacing was observed. The material transforms to the SnS_2 berndtite phase above 200 °C (corresponding to the second mass loss in the TG trace), and further to herzenbergite (SnS) above 300 °C. Heating above 400 °C leads to the formation of cassiterite (SnO_2). At 550 °C, only cassiterite and herzenbergite were detected. As SnO_2 and SnS have the same formula mass, the total mass left at 550 °C can be calculated to be 19% based on the empirical formula $[SnS_{2.07}(HDA)_{2.34}(H_2O)_{2.23}]$ of the material. This is consistent with the observed total mass loss of 81% in the TG trace. The first mass loss of 2.9% in the TG trace corresponds to the partial removal of the occluded water molecules since the total water content in the as-synthesized material is 5.27%. The formation of cassiterite at high temperature suggests that part of the occluded water reacts with the tin(IV) sulfide layers to form SnO_2 and is retained in the solid phase. It is interesting that similar thermal behavior has been observed for microporous layered tin(IV) sulfides.[10] For example, in $(Et_4N)_2Sn_3S_7$, where the pores are built up from six Sn_3S_4 broken-cubes connected together by two double sulfide $(\mu\text{-}S)_2$ bridge bonds, partial removal of these bridging sulfurs above 200 °C through the reaction with the Et_4N^+ template and adsorbed H_2O, induced the rearrangement of the Sn_3S_4 building blocks to that found in the dense-packed layered SnS_2 berndtite. Further removal of the bridging sulfurs and templates results in the formation of herzenbergite and reaction with the occluded water creates cassiterite. The fact that the Meso-SnS-1 follows a very similar thermal transformation pathway is consistent with the proposal that its layers are porous and may be constructed of the same Sn_3S_4 broken-cubes as found in the $(Et_4N)_2Sn_3S_7$ material.

Electrical transport measurements. The conductivity of the as-synthesized Meso-SnS-1 material is determined to be $5.3 \times 10^{-8}\ \Omega^{-1}\ cm^{-1}$ at room temperature, which is about 10^4–10^5 times higher than that of the microporous SnS-*n* materials and comparable to amorphous SnS_2 under identical experimental conditions.[10,23] A preliminary variable-temperature conductivity measurement of Meso-SnS-1 (recorded after temperature cycling between 20 and 110 °C, to ensure a meaningful comparison with the DSC data) shows that the conductivity increases by more than 1000 times from room temperature to 90 °C at which point it behaves as a semiconducting metallomesogen, Fig. 14. The conductivity of mesomorphic tin(IV) sulfide cycles reversibly with temperature and displays interesting discontinuities at the two transition temperatures that correspond to the thermal transitions observed in the DSC trace, Fig. 9. The significant enhancement of conductivity observed on passing from the crystalline to the liquid-crystalline state might originate either from an increase in the interlayer charge transport accompanying the diminished spacing between the tin sulfide layers and/or a reduction of the grain boundary resistance between Meso-SnS-1 particles. Detailed temperature dependent ac/dc conductivity studies will be required to elucidate the electrical properties of this interesting class of organic–inorganic composite materials.

Conclusions

Thermotropic Meso-SnS-1 has been synthesized for the first time and is determined to have a structure based upon porous tin sulfide layers sandwiched with hexadecylamine bilayers, as illustrated in Fig. 3. A thermal transition for Meso-SnS-1 occurs around 45 °C to create a material containing an orientationally ordered alkylamine bilayer with disrupted positional order that is sandwiched between ordered tin(IV) sulfide lamellae. At about 85 °C, this 'semi-liquid crystalline' phase transforms to a fully liquid-crystalline phase containing positionally disordered and orientationally ordered alkylamine bilayers alternating periodically with tin(IV) sulfide lamellae. The registry of the tin(IV) sulfide sheets becomes disrupted at this

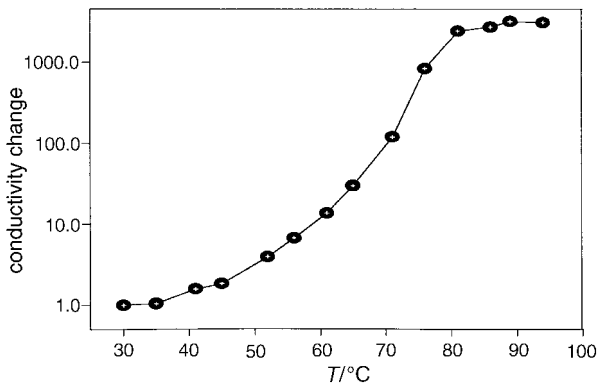

Fig. 14 *In situ* two-probe dc variable-temperature electrical conductivity measurements of Meso-SnS-1 obtained using an interdigitated microelectrode array

temperature. The liquid-crystal phase is best assigned to either a nematic or a smectic C phase. Meso-SnS-1 can be described electrically as a semiconducting metallogen. More detailed studies are necessary in order to elucidate the mechanism of the charge transport of Meso-SnS-1. It is also found that Meso-SnS-1 is able to reversibly adsorb H_2O and CO_2. This indicates that it might be used as a sensing element for a range of molecules with different size, shape and adsorption characteristics. In comparison with the microporous SnS-*n* materials, the advantage of thermotropic Meso-SnS-1 is that it is a better electrical conductor, and most importantly, thin films can be readily fabricated for device applications by simply warming the sample to its liquid-crystalline state. Thin films of the material should provide more sensitive and faster response to analytes.

It is interesting that Meso-SnS-1 is a thermotropic liquid-crystal semiconductor although hexadecylamine itself is a normal crystalline insulator and transforms to an isotropic liquid with heating. It seems that the confinement of hexadecylamine between flexible porous tin sulfide layers hinders certain motions of hexadecylamine and enforces the orientational order of the long molecule axes. A whole new family of tin sulfide-based metallogens can be envisaged by varying the length, shape and charge of amine guest molecules. They are expected to yield different porous tin sulfide layer structures and interlamellar spacings, thus creating different LC behavior and temperature ranges. In addition, when the same starting reaction mixture of Meso-SnS-1 is crystallized at room temperature for 19 days, a white material, denoted Meso-SnS-2, is obtained whose PXRD and DSC traces are displayed in Fig. 15. It shows a distinct PXRD pattern and thermal behaviour in comparison with the Meso-SnS-1 phase. In addition, there is only one chemical shift observed at $\delta -390$ relative to $SnMe_4$ in its ^{119}Sn solid-state MAS NMR spectrum. All of this suggests the material is built-up of a single kind of five-coordinate tin(IV) site and has a distinct structure compared with Meso-SnS-1. This clearly demonstrates that many new tin sulfide-based mesomorphic materials can be formed. Although it is difficult to be explicit about the development of potential device applications for this new class of thermotropic liquid crystals, one can envisage that their intrinsic semiconducting and metallomesogenic character could possibly simplify the fabrication of certain types of liquid-crystal displays. To amplify, a single layer of our bifunctional material could replace the conventional bilayer device requirement of an electrically conducting contact layer organized adjacent to a liquid-crystal layer. Also, because of the highly open and flexible structures of these materials it may prove possible to develop a range of small and large molecule discriminating semiconducting metallomesogenic chemical sensors.

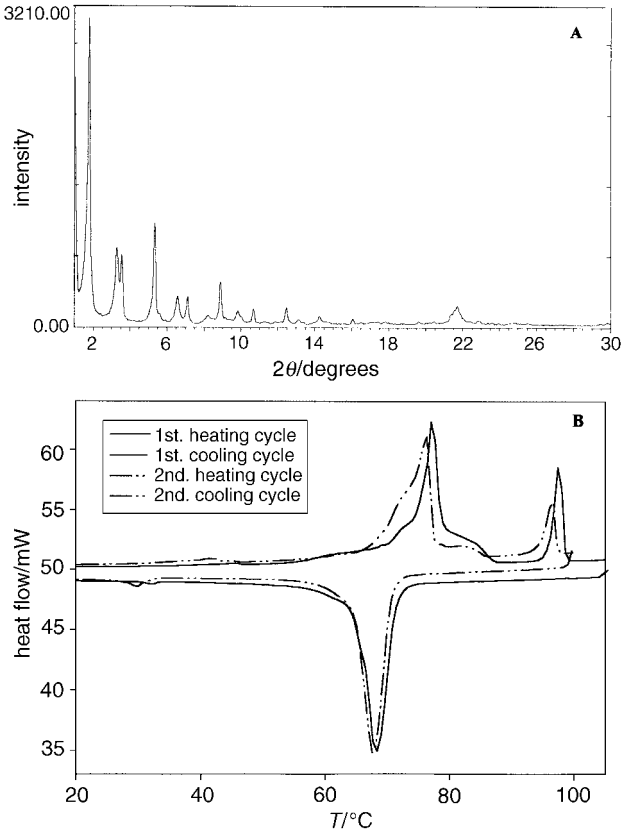

Fig. 15 (A) PXRD pattern and (B) DSC trace of Meso-SnS-2

Experimental

Reagents

$SnCl_4 \cdot 5H_2O$, $(NH_4)_2S$ (20% aqueous solution), ammonia aqueous solution (28%) and hexadecylamine (90%) were purchased from Aldrich and used directly for synthesis without further purification.

Synthesis

The optimized reaction mixture for the synthesis of phase pure Meso-SnS-1 has a starting composition of 2.6 $C_{16}H_{33}NH_2$: 260 H_2O : 16 NH_4OH : 2 $(NH_4)_2S$: $SnCl_4$.

To the gel of hexadecylamine and water, an aqueous ammonia solution was added and well stirred. Aqueous ammonium sulfide and then tin tetrachloride solutions were added with stirring. A yellow precipitate was formed immediately which slowly transformed to a homogeous light yellow gel with vigorous stirring. The resulting gel was sealed in a teflon-lined stainless-steel reactor and crystallized at 150 °C for 19 h. A yellow product was formed which interestingly had aggregated together in a single cylinder shape standing in the middle of the liner. It was recovered by washing with a large quantity of water and acetone, and dried in air. The product is found to be hydrophobic and repels water.

Physical measurements

Both room- and *in situ* variable-temperature-powder X-ray diffraction (PXRD) patterns were collected on a Siemens D-5000 diffractometer with Cu-Kα radiation. For high-temperature PXRD measurements, the sample was placed on a flat Pt strip and held in place by a very thin layer of silicone grease. The PXRD data collection was performed under a flow of nitrogen with a heating rate of 10 °C min^{-1}. The temperature was held constant during data collection.

Scanning electron micrograph (SEM) images were recorded using a Hitachi S-570 microscope with an accelerating voltage of 20 kV. Transmission electron micrograph (TEM) images were obtained using Philips 430 microscope, operating at 100 kV. An extremely thin crystal edge of an as-synthesized sample was directly used to obtain a TEM image of the sheets without microtoming. Epoxy embedding and microtoming of samples was required to obtain a TEM image orthogonal to the lamellae. Raman spectra were collected on a Bomens MB-157 Fourier-transform spectrometer using a Spectra Physics diode-pumped Nd:YLF laser emitting at 1064 nm. UV–VIS diffuse reflectance spectra were obtained using a Cary 3 spectrometer and transformed to absorption by using the Kubelka–Munk transformation. Solid-state ^{119}Sn NMR spectra were recorded using a Bruker DSX 200 MHz spectrometer while ^{13}C and ^{15}N MAS NMR spectra were obtained on a Bruker DSX 400 spectrometer. Samples were packed into 4 mm zirconium rotors. Samples for Mössbauer spectroscopy were packed and sealed in circular plastic disk sample holders. Mössbauer spectra were recorded at room temperature on a

Ranger Scientific MS-200 instrument in a constant acceleration mode. The γ-ray source used was 5 mCi of ^{119}Sn in a $CaSnO_3$ matrix. Isomer shift values obtained were referenced to SnO_2 (0.0 mm s^{-1}).

Thermogravimetry (TG) data were obtained using a Perkin-Elmer TGA7 under a flow of nitrogen with a heating rate of 5 °C min^{-1}. Differential scanning calorimetry (DSC) was performed using a Perkin-Elmer DSC 7 under a nitrogen flow with a heating rate of 5 °C min^{-1}, the sample being sealed in an aluminum sample holder. Optical images were recorded using an Olympus polarizing optical microscope equipped with a Mettler FP82 hot stage and FP80 central processor. Room-temperature electrical conductivity measurements were performed using a four-probe dc technique. The sample was pressed into a rectangular shaped bar with dimensions of $0.5 \times 0.5 \times 1$ cm^3. *In situ* variable-temperature electrical conductivity measurements were obtained using an interdigitated microelectrode array in a controlled atmosphere chamber capable of subjecting the samples to high vacuum or known pressures of the vapours of different gaseous species. A uniform film was created by heating a powder sample to the melting temperature and pressing gently with a cover slide. Electrode contacts were made of gold to avoid Schottky barrier effects.

The financial assistance of the Natural Sciences and Engineering Research Council of Canada (NSERC) is deeply appreciated. Insightful discussions with Dr. Robert Bedard at UOP proved to be most helpful. The assistance of Dr. Walter Zamachek at UOP with elemental analysis was invaluable. We would like to thank Dr. Patricia Aroca for her expert help with the collection of solid-state NMR spectra and Dr. Ömer Dag for his assistance with FT-Raman measurements. Ms. Cathy Liu was most helpful with the hot-stage polarized optical microscopy measurements and many stimulating discussions on optical birefringence textures of liquid crystals. Dr. Neil Coombs of Imagetec provided the SEM and TEM images and Dr. Atul Verma recorded the electrical conductivity data. Dr. Srebri Petrov assisted with variable-temperature PXRD experiments. Early work on surfactant-templated tin sulfide materials synthesis conducted in this laboratory by Mr. Philip Britz-McKibbin, Dr. David Young and Dr. Alex Kuperman provided inspiration for this work.

References

1 D. Demus and K. Hiltrop, in *Liquid Crystals*, ed. H. Stegemeyer, Dr. Dietrich Steinkopff Verlag GmbH & Co. KG, Darmstadt, 1994.
2 (*a*) F. Reinitzer, *Monatsh. Chem*., 1888, **9**, 421; (*b*) O. Lehmann, *Die Flussige Kristalle*, Akademische Verlags-gesellshaft M.B.H., Liepzig, 1911.
3 M. Freemantle, *Chem. Eng. News*, 1996, Dec. 16, 33.
4 (*a*) *Liquid Crystals: Applications and Uses*, ed. B. Bahadur, World Scientific, Singapore, 1991 vol. 1–5; (*b*) L. M. Blinov and V. G. Chigrinov, *Electrooptic Effects in Liquid Crystal Materials*, Springer, Berlin, 1994.
5 D. Demus and L. Richter, *Textures of Liquid Crystals*, Verlag Chemie, New York, 1978.
6 (*a*) A. M. Donald and A. H. Windle, *Liquid Crystalline Polymers*, Cambridge University Press, Cambridge, 1992; *Polymer Liquid Crystals*, ed. A. Ceferri, W. R. Krigbaum and R. B. Meyer, Academic Press, New York, 1982.
7 (*a*) V. Percec, P. Chu, G. Ungar and J. Zhou, *J. Am. Chem. Soc*., 1995, **117**, 11441; (*b*) K. Lorenz, D. Hölter, B. Stühn, R. Mülhaupt and H. Frey, *Adv. Mater*., 1996, **6**, 414.
8 D. W. Bruce, in *Inorganic Materials*, ed. D. W. Bruce and D. O'Hare, Wiley, Chichester, UK, 1992.
9 F. Neve, *Adv. Mater*., 1996, **8**, 277.
10 (*a*) T. Jiang, G. A. Ozin and R. L. Bedard, *Adv. Mater*., 1995, **7**, 166; (*b*) T. Jiang, Ph.D. Thesis, University of Toronto, 1997.
11 (*a*) T. Jiang, G. A. Ozin and R. L. Bedard, *Chem. Mater*., 1995, **7**, 245; (*b*) C. L. Bowes and G. A. Ozin, *Adv. Mater*., 1996, **8**, 13 and references therein.
12 (*a*) H. P. B. Rimmington and A. A. Balchin, *J. Cryst. Growth*, 1972, **15**, 51; (*b*) B. Palosz, W. Steurer and H. Schulz, *Acta Crystallogr., Sect. B*, 1990, **46**, 449.
13 W. S. Sheldrick, *Z. Anorg. Allg. Chem*., 1988, **562**, 23.
14 F. R. Gamble, J. H. Osiecki, M. Cais, R. Pisharody, F. J. DiSalvo and T. H. Geballe, *Science*, 1971, **174**, 493.
15 A. J. Jacobson, in *Intercalation Chemistry*, ed. M. S. Whittingham and A. J. Jacobson. Academic Press, New York, 1982, p. 239.
16 (*a*) A. Crispini, M. Ghedini, S. Morrone, D. Pucci and O. Francescangeli, *Liq. Cryst*., 1996, **20**, 67; (*b*) A. De Vries, *Mol. Cryst. Liq. Cryst*., 1985, **131**, 125; (*c*) K. M. Lee, C. K. Lee and I. J. B. Lin, *Chem. Commun*., 1997, 899.
17 F. R. Gamble, F. J. Disalvo, R. A. Klemm and T. H. Geballe, *Science*, 1970, **168**, 568.
18 M. B. Dines, *Inorg. Chem*., 1978, **17**, 763.
19 (*a*) D. Dakternieks, H. Zhu, D. Masi and C. Mealli, *Inorg. Chem*., 1992, **31**, 3601; (*b*) R. Hani and R. A. Geanangel, *Coord. Chem. Rev*., 1982, **44**, 229; (*c*) C. Mundus, G. Taillades, A. Pradel and M. Ribes. *Solid State Nucl. Magn. Reson*., 1996, **7**, 141.
20 J.-C. Jumas, E. Philippot and M. Maurd, *J. Solid State Chem*., 1975, **14**, 152.
21 (*a*) J. Robertson, *J. Phys. C: Solid State Phys.* 1979, **12**, 4735; (*b*) E. Lifshitz, Z. Chen and L. Bykov, *J. Phys. Chem*., 1993, **97**, 238.
22 (*a*) E. A. Axtell III, J.-H. Liao, Z. Pikramenou and M. G. Kanatzidis, *Chem. Eur. J*., 1996, **2**, 656; (*b*) E. A. Axtell III, J.-H. Liao, Z. Pikramenou, Y. Park and M. G. Kanatzidis, *J. Am. Chem. Soc*., 1993, **115**, 12 191.
23 G. A. Ozin, C. L. Bowes, T. Jiang, A. Lough, S. Petrov, G. Vovk, A. Verma and D. Young, Electrical Sieves for Molecular Recognition, *Proceedings of 9th. International Symposium on Molecular Recognition and Inclusion, November 1996*, ed. A. Coleman, Lyon, France, Kluwer Academic Publications, Dordrecht, 1997.

Paper 7/03069J; *Received* 6*th May*, 1997